


Article

Three-Dimensional Structural Analysis of Ferromanganese Nodules from the Western North Pacific Ocean Using X-ray Computed Tomography

Kentaro Nakamura ^{1,2,*}, Daiki Terauchi ¹, Ryo Shimomura ¹, Shiki Machida ^{2,3}, Kazutaka Yasukawa ^{1,3} , Koichiro Fujinaga ^{2,3} and Yasuhiro Kato ^{1,2,3}

- ¹ Department of Systems Innovation, School of Engineering, The University of Tokyo, 7-3-1 Hongo, Bunkyo-ku, Tokyo 113-8656, Japan; gantyan612@gmail.com (D.T.); rshimomura58@gmail.com (R.S.); k-yasukawa@sys.t.u-tokyo.ac.jp (K.Y.); ykato@sys.t.u-tokyo.ac.jp (Y.K.)
- ² Ocean Resources Research Center for Next Generation (ORCeNG), Chiba Institute of Technology, 2-17-1 Tsudanuma, Narashino, Chiba 275-0016, Japan; shiki.machida@p.chibakoudai.jp (S.M.); k-fujinaga@sys.t.u-tokyo.ac.jp (K.F.)
- ³ Frontier Research Center for Energy and Resources (FRCER), School of Engineering, The University of Tokyo, 7-3-1 Hongo, Bunkyo-ku, Tokyo 113-8656, Japan
- * Correspondence: kentaron@sys.t.u-tokyo.ac.jp; Tel.: +81-3-5841-7089

Abstract: The three-dimensional layered growth structure of 934 ferromanganese nodule samples collected from dives in the Pacific Ocean around Minamitorishima Island was assessed using X-ray computed tomography (X-ray CT) to elucidate their growth history. The thickness of the layered structure measured in three orthogonal directions showed that the ferromanganese nodules grew equally in all directions regardless of shape and size. Based on differences in CT numbers, a layered structure was subdivided into sublayers I, II, III, and IV, which corresponded to petrological features. The nodules were then classified as Types I, II, III, and IV according to whether they had sublayers I, I and II, I–III, or I–IV, respectively. Correlations between the total thickness of the layers and the number of sublayers indicated that both represented the relative age of the nodules. Nodules with all these types were recovered from most of the sampling sites, and histograms of the total layer thickness at each dive site showed several peaks. These findings indicated that the initiation of nodule growth was intermittent, rather than simultaneous. Three distinct thickness peaks were found at many sites throughout the study area, suggesting that at least three nodule initiation events covering hundreds of kilometers initiated the growth of ferromanganese nodules.

Keywords: ferromanganese nodule; X-ray computed tomography; Minamitorishima Island



Citation: Nakamura, K.; Terauchi, D.; Shimomura, R.; Machida, S.; Yasukawa, K.; Fujinaga, K.; Kato, Y. Three-Dimensional Structural Analysis of Ferromanganese Nodules from the Western North Pacific Ocean Using X-ray Computed Tomography. *Minerals* **2021**, *11*, 1100. <https://doi.org/10.3390/min11101100>

Academic Editor: Francisco J. González

Received: 22 September 2021

Accepted: 5 October 2021

Published: 7 October 2021

Publisher's Note: MDPI stays neutral with regard to jurisdictional claims in published maps and institutional affiliations.



Copyright: © 2021 by the authors. Licensee MDPI, Basel, Switzerland. This article is an open access article distributed under the terms and conditions of the Creative Commons Attribution (CC BY) license (<https://creativecommons.org/licenses/by/4.0/>).

1. Introduction

Spherical ferromanganese nodules composed of iron (Fe) and manganese (Mn) oxides and hydroxides are widely distributed on the deep seafloor [1–3]. These nodules are also enriched in critical metals such as nickel (Ni), copper (Cu), cobalt (Co), and rare-earth elements (REEs), representing a potential resource of the metals that are crucial for high-tech and green-tech products [2,4]. To date, large nodule fields have been identified in the Clarion-Clipperton Zone (CCZ), the Peru Basin, the Penrhyn-Samoa basins, and the Central Indian Ocean Basin [1,3,5–8]. Ferromanganese nodules in the CCZ have attracted economic interest due to their wide distribution and high concentration of Cu and Ni, and this nodule field has been extensively investigated over the past several decades [1,3,5,9–11]. A large field of ferromanganese nodules has recently been discovered in the Japanese Exclusive Economic Zone (EEZ) around Minamitorishima Island in the western North Pacific Ocean [12,13]. Machida et al. [12] revealed that the nodules are characterized by high concentrations of Co, Ni, and Cu, and determined that they have potential as a metal resource.

Ferromanganese nodules have layered growth structures (oxide layers) formed by the accumulation of Fe-Mn oxides/hydroxides around a nucleus like the rings of trees. The nodules from the Minamitorishima EEZ generally consist of concentric layers, L0, L1, and L2 that are comparable to those of ferromanganese crusts in the western North Pacific, including the Minamitorishima EEZ [12]. As the layered structures reflect nodule growth history, a detailed study of the structure is an important key to understanding how they are formed. However, the three-dimensional structure of ferromanganese nodules has not been comprehensively investigated because the nodules need to be cut at multiple locations for observation; thus, observing a large number of nodules is laborious, costly, and impractical.

The three-dimensional internal structure of geological samples can now be determined without destroying samples due to recent advances in X-ray computed tomography (CT) [14–16], and it has also been applied to ferromanganese nodules [17,18]. The three-dimensional structures of numerous ferromanganese nodules should provide new insights into the ore genesis of the nodules. Therefore, the present study used X-ray CT to determine the three-dimensional structure of the oxide layer of 934 ferromanganese nodule samples collected from the western North Pacific Ocean around Minamitorishima Island.

2. Materials and Methods

2.1. Sample Collection

Nodules were collected by 16 dives using the deep-sea manned submersible Shinkai 6500 within and near the Minamitorishima EEZ during the YK16-01 and YK17-11C cruises of the R/V Yokosuka during 2016 and 2017, respectively (Figure 1). Ferromanganese nodules were sampled at two to six points each from 13 of the 16 dive sites (Figure 1) using a manipulator, scoop, and push cores. Some relatively large samples were collected by targeted sampling using the manipulator arm of the Shinkai 6500 (Figure 2A). Most samples were collected Nodules were collected by 16 dives using the deep-sea manned submersible Shinkai 6500 within and near the Minamitorishima EEZ during the YK16-01 and YK17-11C cruises of the R/V Yokosuka during 2016 and 2017, respectively (Figure 1). Ferromanganese nodules were sampled at two to six points each from 13 of the 16 dive sites (Figure 1) using a manipulator, scoop, and push cores. Some relatively large samples were collected by targeted sampling using the manipulator arm of the Shinkai 6500 (Figure 2A).

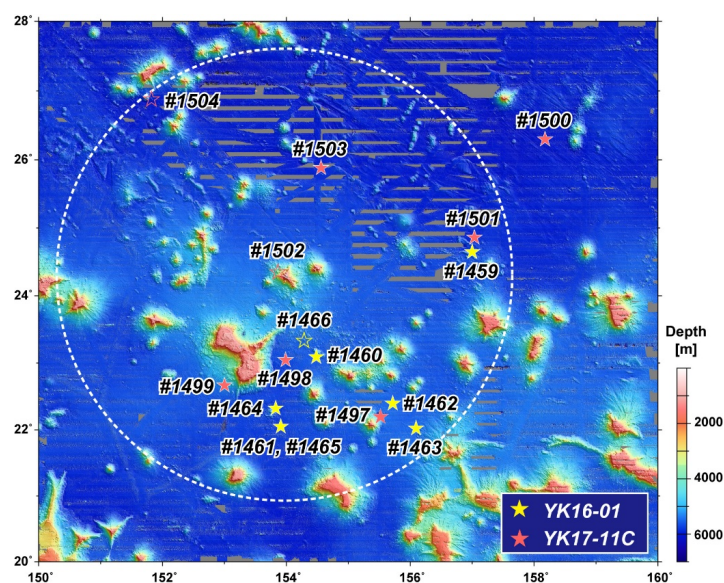


Figure 1. Bathymetric map shows locations of SHINKAI 6500 dive sites during cruises YK16-01 and YK17-11C of R/V Yokosuka. Filled stars indicate sites where ferromanganese nodules were collected; blank stars show sites where nodules were not sampled. Dashed white circle represents Japanese exclusive economic zone.

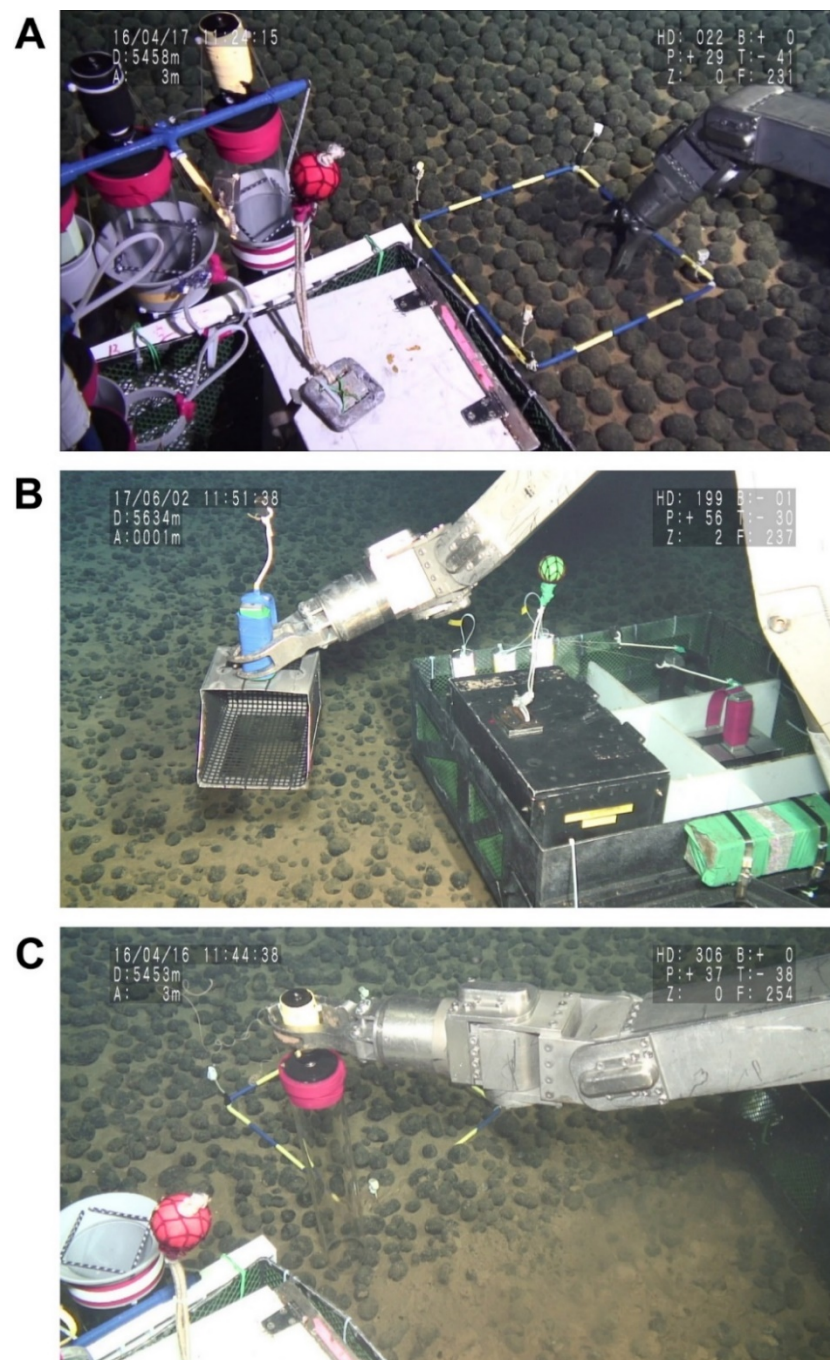


Figure 2. Photographs show ferromanganese nodules sampling using (A) manipulator, (B) scoop, and (C) push core.

Most samples were using a scoop (Figure 2B) to obtain nodules of various sizes without bias. However, sampling with a scoop was impossible when adjacent nodules were connected or when the underside of a nodule adhered to sediment. Several nodule samples were collected using push cores together with sediment samples (Figure 2C). Nodules collected using push cores were in the same vertical orientation as they were when deposited on the seafloor. Table 1 summarizes the latitude, longitude, and water depth location of each sampled point and describes the sampling tools.

Table 1. Locations of the sampling points and employed sampling tools during YK16-01 and YK17-11C cruises.

Dive	Stop	Depth (mbsl)	Location		Sampling Tools
			Latitude (N)	Longitude (E)	
6K#1459	1	5499	24°35.70'	157°00.98'	M, S
	2	5485	24°35.55'	157°00.88'	M
	3	5590	24°33.63'	156°59.66'	S
	4	5503	24°34.36'	157°00.49'	S
	5	5565	24°33.99'	156°59.98'	P
6K#1460	1	5531	23°05.02'	154°26.55'	M
	2	5549	23°04.96'	154°25.36'	M
6K#1461	1	5730	21°59.05'	153°56.33'	M, S, P
	2	5731	21°59.00'	153°56.02'	S, P
6K#1462	1	5456	22°19.91'	155°44.06'	M, S, P
	2	5455	22°19.03'	155°43.17'	-
	3	5458	22°18.89'	155°43.13'	M, P
	4	5446	22°18.34'	155°42.50'	M, S, P
	5	5445	22°18.18'	155°42.27'	S, P
6K#1463	1	5461	21°57.15'	156°06.64'	M, P
	2	5459	21°57.08'	156°06.77'	S
	3	5289	21°56.83'	156°07.81'	S
	4	5190	21°56.82'	156°08.03'	S, P
	5	5030	21°56.77'	156°08.27'	S
6K#1464	1	5781	22°15.43'	153°51.38'	M, S, P
	2	5785	22°15.14'	153°51.66'	M
	3	5785	22°14.79'	153°52.26'	S, P
	4	5755	22°14.77'	153°53.17'	S, P
	5	5759	22°14.76'	153°53.42'	S, P
	6	5763	22°14.78'	153°53.84'	S
6K#1465	1	5729	21°59.11'	153°56.32'	S
	2	5725	21°59.70'	153°56.30'	P
	3	5696	22°01.12'	153°56.29'	M
	4	5685	22°01.68'	153°56.29'	M, S, P
6K#1497	1	5163	22°07.88'	155°32.51'	M, S, P
	2	4936	22°07.57'	155°30.62'	S, P
	3	4847	22°07.64'	155°30.20'	M, S
6K#1498	1	5639	22°59.01'	154°00.94'	M, S, P
	2	5644	22°57.97'	154°00.51'	M, S
	3	5657	22°57.20'	154°00.21'	M, S
	4	5686	22°56.74'	153°59.84'	S, P
6K#1499	1	5264	22°36.26'	153°02.03'	S, P
	2	5085	22°38.42'	153°02.07'	-
	3	5001	22°38.49'	153°02.10'	-
	4	4966	22°38.60'	153°02.17'	S, P
6K#1500	1	6066	26°15.06'	158°11.03'	S, P
	2	6046	26°15.35'	158°11.37'	M
	3	6034	26°15.51'	158°11.61'	S, P
	4	6013	26°16.14'	158°12.32'	M
	5	6015	26°16.11'	158°12.48'	M
6K#1501	1	5866	24°48.64'	157°02.79'	S, P
	2	5861	24°47.30'	157°02.69'	M, S, P
	3	5871	24°47.67'	157°02.04'	S
	4	5838	24°47.59'	157°01.56'	S
6K#1503	1	5860	25°49.99'	154°35.08'	P
	2	5849	25°48.71'	154°34.80'	P
	3	5866	25°48.16'	154°34.69'	S, P
	4	5736	25°47.28'	154°34.55'	P

mbsl: meters below sea level. M = manipulator; S = scoop; P = push corer; - = nodules were not sampled.

2.2. Analytical Method

The internal structure of Mn-nodule samples was analyzed using LightSpeed Ultra 16 X-ray CT scanner (GE Healthcare, Chicago, IL, USA) for samples from 6 K #1459, 1460, 1461, 1462, 1463, and 1464 (YK16-01) and an Aquilion PRIME/Focus Edition X-ray CT scanner (Canon Medical Systems Corp., Otawara, Japan) for samples from 6 K #1465 (YK16-01), 1497, 1498, 1499, 1500, 1501, and 1503 (YK17-11C) at the Center for Advanced Marine Core Research, Kochi University (Kochi, Japan). The samples were analyzed by both scanners operating at 120 kV and 100-mA. The signal at each point in the images (CT number) is expressed as Hounsfield units (HU) and is defined as,

$$\text{CT number} = 1000 \frac{\mu - \mu_w}{\mu_w} [\text{HU}]$$

where μ and μ_w are the linear X-ray absorption coefficients, respectively, of the sample and pure water, which was the standard reference. As the degree of X-ray attenuation depends on the density and atomic number of the samples, the CT number can be regarded as a function of the porosity and chemical composition of the material in any voxel. Details of the principles of X-ray CT imaging are provided elsewhere [14,19–24].

After excluding broken or severely damaged ferromanganese nodules, we measured the thickness of the oxide layer in 934 nodules using the open-source Digital Imaging and Communication in Medicine (DICOM) software OsiriX [25], that can reliably measure length on CT images with accuracy <0.3 mm which is a viable alternative to actual measurements [26]. The thickness of the oxide layer was measured along three mutually orthogonal axes through the nucleus, each of which was measured twice ($n = 6$ measurements per sample) (Figure 3). We also measured the long, middle, and short axes using a caliper. These three axes did not strictly correspond to those along which the thickness of the oxide layer was measured.

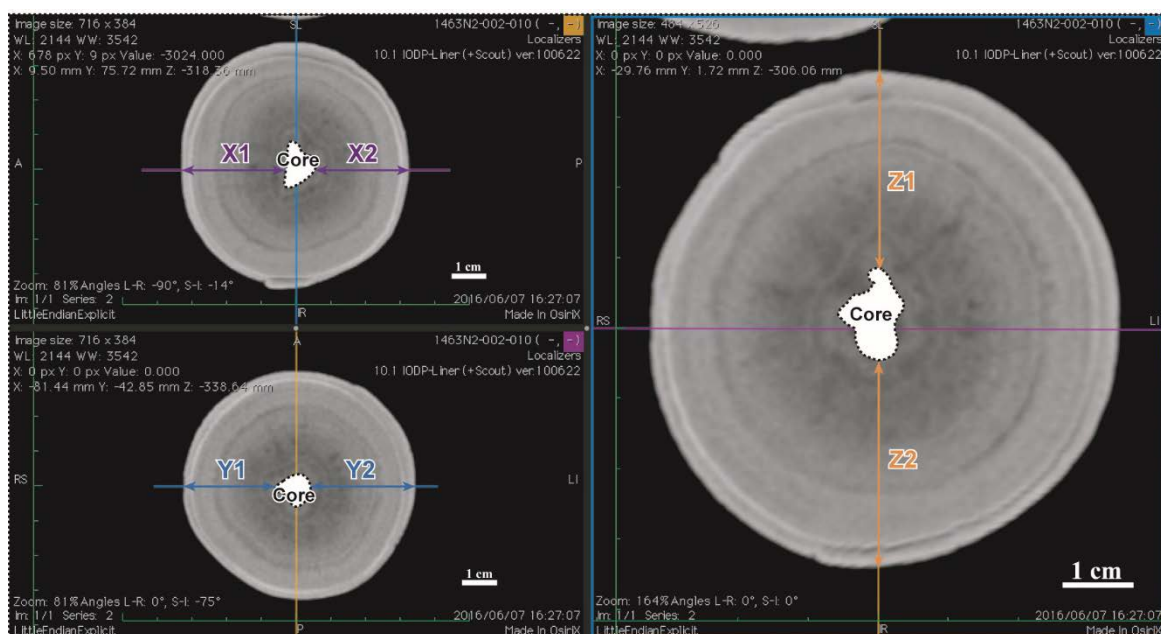


Figure 3. Computed tomography images of representative ferromanganese nodule show oxide layer thickness (sample 6K#1463N2-007). Directions X, Y, and Z are orthogonal to each other. Oxide layer thickness was measured at two points along each of these directions.

3. Results and Discussion

3.1. Relationship between Oxide Layer Thickness and Nodule Size

The thickness of the oxide layer and nodule size are summarized in Table S1. Figure 4 shows the thickness of the oxide layer in the X, Y, and Z axes, and the thickness of the oxide layer in these directions was the average of the measurements at two points on the sides of each axis (Figure 3). The thickness of the oxide layers along the three axes closely correlated, and the regression line tended to be consistent with the 1:1 line. These results indicated that the oxide layer of the nodules at the study site grew uniformly, regardless of the direction, although some samples deviated from the regression line.

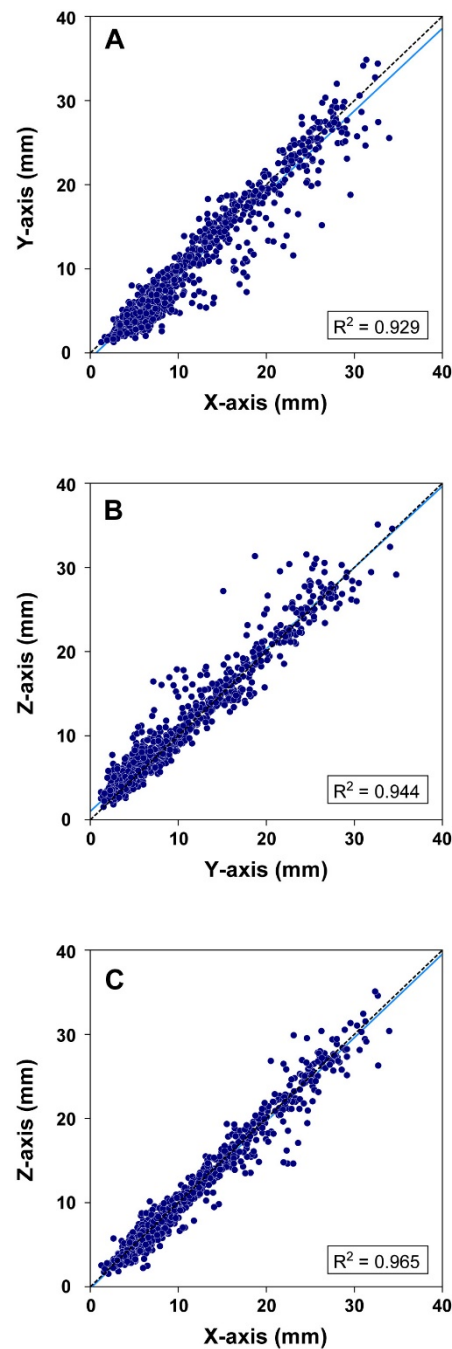


Figure 4. Scatter plots show relationships between averaged oxide layer thicknesses along axes (A) Y and X, (B) Z and Y, and (C) Z and X. Dashed black lines, 1:1; blue solid lines, least square regression lines. Coefficients of determination (R²) are also shown.

Figure 5 shows the relationships between the total thickness of the oxide layer and nodule size. Total oxide layer thickness was determined by averaging the two values measured along the three axes, although parameters could not be measured in some damaged samples (Table S1). All graphs show good positive correlations, indicating that the size of the nodules is mainly controlled by the thickness of the oxide layer. Considering that the oxide layer grew evenly in all directions, we considered that the shape of the ferromanganese nodules primarily reflects that of their nuclei, and that the y-intercept values indicate the average size of the nuclei ($\sim 14 \times 9 \times 4$ mm).

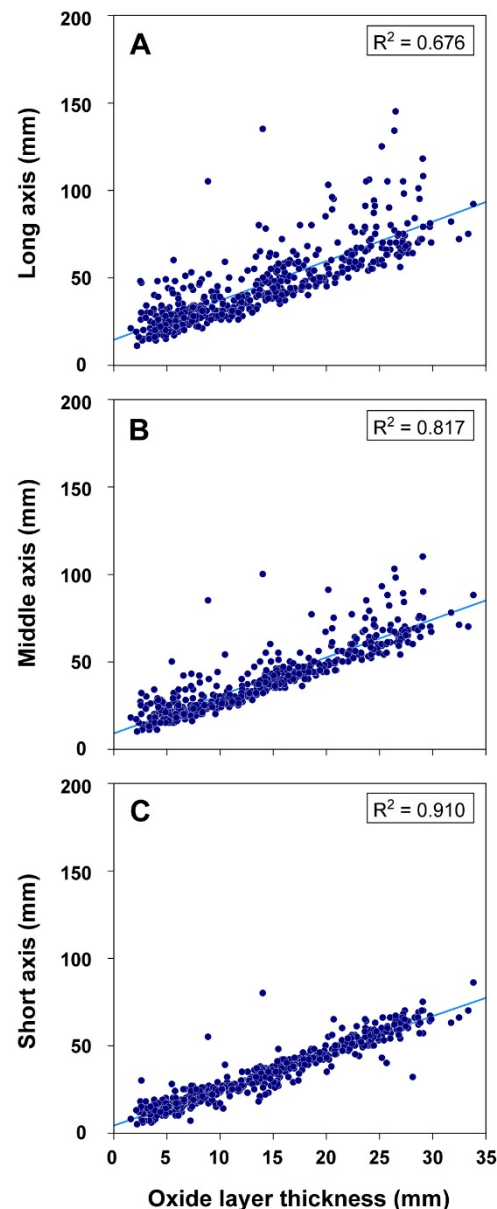


Figure 5. Scatter plots show relationships between averaged oxide layer thickness determined by X-ray CT and nodule size (long axis (A), middle axis (B), and short axis (C)) measured using caliper. The least square regression lines (blue solid lines) and the coefficients of determination (R^2) are also shown.

Some samples with large nuclei significantly deviated from the regression lines in plots of oxide layer thickness vs. long (Figure 5A) and middle (Figure 5B) axes. In contrast, the thickness of the oxide layer correlated very well with the short axis (Figure 5C). Therefore, the short axis is the more practical indicator (rather than the longer axis or the average of

all axes) when comparing the thickness of the oxide layer of ferromanganese nodules on board a ship.

3.2. Classification of Layers Based on CT Numbers

Based on the three-dimensional distribution of CT numbers, the oxide layer of the ferromanganese nodules can be subdivided into sublayers, I, II, III, and IV, from the surface to the nucleus. The sublayers I, II, III, and IV are defined by the dominance of CT numbers >2600, 2300–2600, 2000–2300, and < 2000 HU, respectively (Figure 6A). The sublayer boundaries were determined based on the fact that the change in the CT number at the boundary was larger than the variation within each sublayer (Figure 6A). The porosity of the nodules was not only controlled by the growth structure of the manganese minerals but also by other structural disturbances such as cracks and cavities. Therefore, these structural disturbances result in inconsistent CT numbers (Figure 7F,G,L,P).

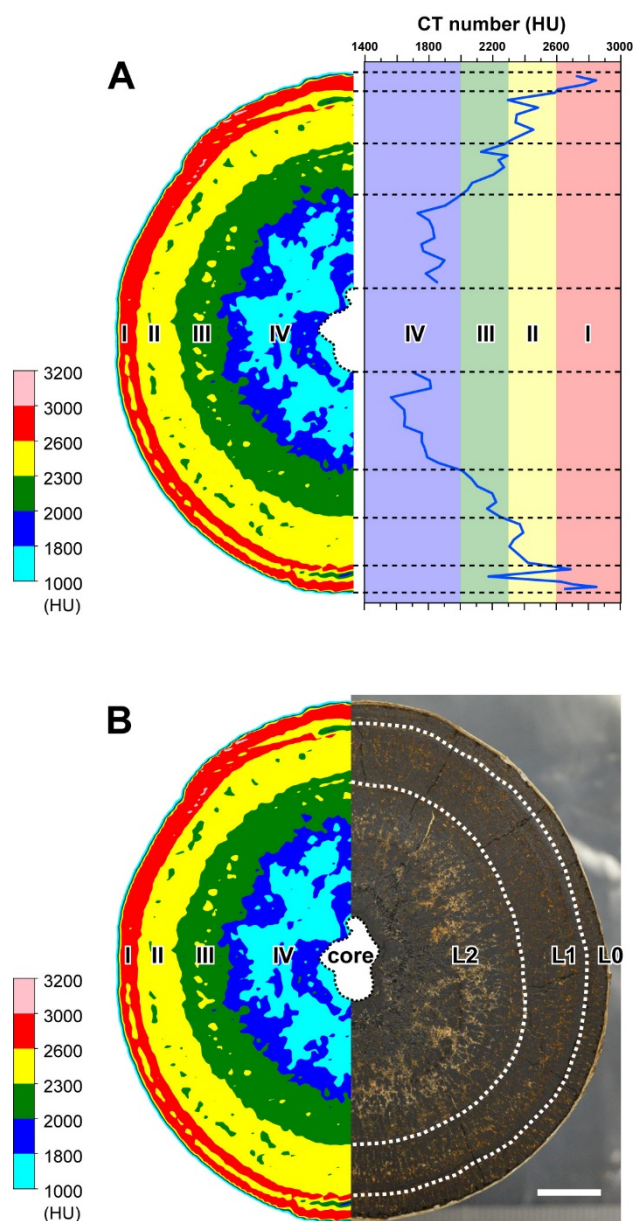


Figure 6. Comparison with contour plot of CT numbers (left half) and (A) line profile of CT number and (B) photograph of representative ferromanganese nodule sample 6K#1463N2-007. Dashed white lines (B) represent layer boundaries defined by petrological findings Machida et al. [12].

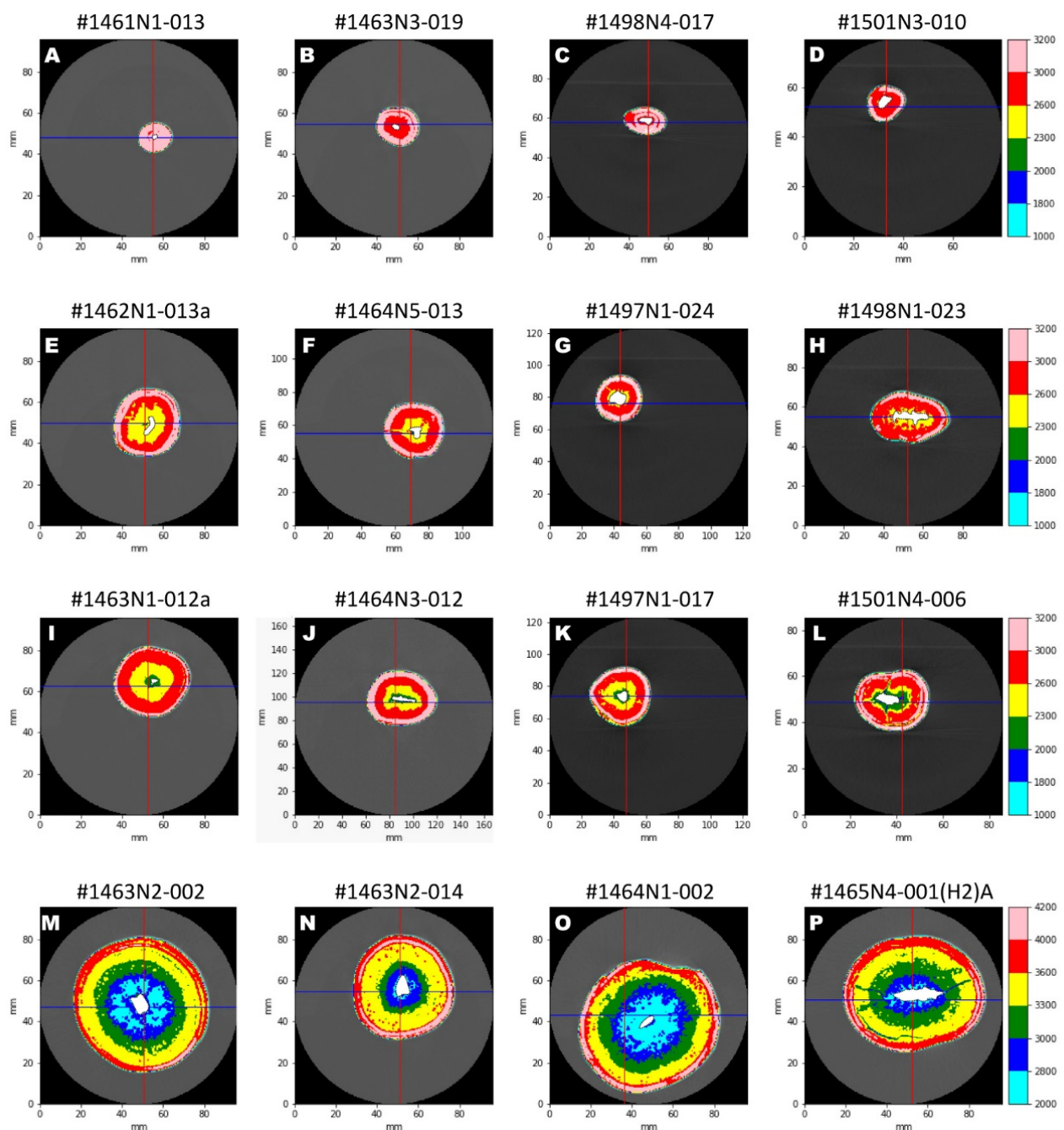


Figure 7. Contour plots of CT numbers for representative samples having sublayer I (A–D), sublayers I and II (E–H), sublayers I–III (I–L), and I–IV (M–P).

Different CT numbers for each sublayer could generally reflect differences in porosity, because the degree of X-ray attenuation largely depends on the density. Thus, systematic changes in CT numbers from the inner, to the outer sublayer indicated that nodule porosity decreases from the inside to the outside. Furthermore, changes in porosity subsequently corresponded to difference in petrographic features within the oxide layer, reflecting a shift in the formation environment.

Sublayer IV seemed to be further subdivided into parts with relatively higher and lower CT values (1800–2000 vs. <1800 HU). However, the two portions were not layered and intricately interrelated, although the boundary with sublayer III was dominated by the part with the relatively higher HU (Figures 6 and 7M–P). These findings suggested that the difference between the parts in sublayer IV with high- and low-HU are attributable

to structural heterogeneity within this sublayer rather than the layered structure of the nodules. Indeed, Figure 6B shows that the structure of this sublayer is porous and heterogeneous. Sublayer I also seemed to comprise parts with relatively high and low CT numbers (>3000 vs. 2600–3000 HU). Some samples had inner and outer portions with lower and higher CT numbers, respectively that apparently constituted a layered structure (Figure 7B,D–G,I–K). In contrast, the portions with the higher and lower HU were intricately mixed in other samples (Figure 7C,H,L–P), suggesting that the two portions were not layered, like sublayer IV. Thus, we regarded the two portions as one sublayer (sublayer I), although the structural and genetic relationships between them are not clear yet.

Machida et al. [12] noted based on petrographic findings of two half-cut samples that nodules from the Minamitorishima EEZ generally consist of a concentric outermost mottled layer (L0), a massive black layer (L1), and an innermost porous layer (L2). The present findings agreed with these results (Figure 6B). The present X-ray CT results showed that sublayers I and II were comparable to the L0 and L1 layers, respectively (Figure 6B), and that sublayers III and IV were comparable to the L2 layer (Figure 6B). Consequently, the layered structure identified by X-ray CT closely corresponded to that defined based on petrographic features, reflecting that changes in CT numbers are generally attributable to those in visible petrographic textures. The L2 identified by Machida et al. [12] was further subdivided into sublayers III and IV by the present X-ray CT findings (Figure 6B), indicating that X-ray CT can identify changes in rock texture that petrological analyses cannot clearly identify. Therefore, we concluded that X-ray CT is an efficient, effective, and non-destructive way to reveal more petrological details about numerous ferromanganese nodule samples.

Machida et al. [27] further classified three layers that they previously defined [12] into nine sublayers using μ -XRF multi element mapping. They showed that the L0, L1, and L2 layers can be subdivided into two (L0 inner, L0 outer), three (L1 inner, L1 middle, L1 outer), and four (L2 inner, L2 middle, L2 outer, L2 outermost) sublayers, respectively, based on the distribution of Fe, Mn, Ti, Si, P, and Cu. X-ray CT did not discern further sublayers in the L0 and L1 layers. Although X-ray CT recognized that the L2 layer comprised two sublayers, the four sublayers identified by Machida et al. [27] were not clearly visualized. Whereas X-ray CT identified density changes that reflect changes in rock structures, μ -XRF chemical mapping detects changes in the composition of multiple elements. This could result in the recognition of changes in the depositional environment that are not apparent in changes in rock structure, leading to the identification of more layers compared with petrological and X-ray CT analyses. Consequently, the μ -XRF mapping proposed by Machida et al. [27] can analyze the oxide layer in more detail, but it still requires cutting nodule samples in half.

3.3. Implications for the History and Trigger of Nodule Growth

The ferromanganese nodules were subdivided into types I, II, III, and IV depending on whether they had only sublayer I, sublayers I and II, I–III, or I–IV) (Figure 7). None of the samples had more missing outer layers than the innermost sublayer. This suggests that none of the nodules had ever been affected by any event during their lifetime that resulted in the complete loss of one or more sublayers. Therefore, we considered that the difference in the number of sublayers represents the time when a nodule began to grow. Moreover, samples with more sublayers tended to have a thicker oxide layer (Figure 8). Therefore, the total thickness of the oxide layer and the number of sublayers might indicate the relative age of the nodule.

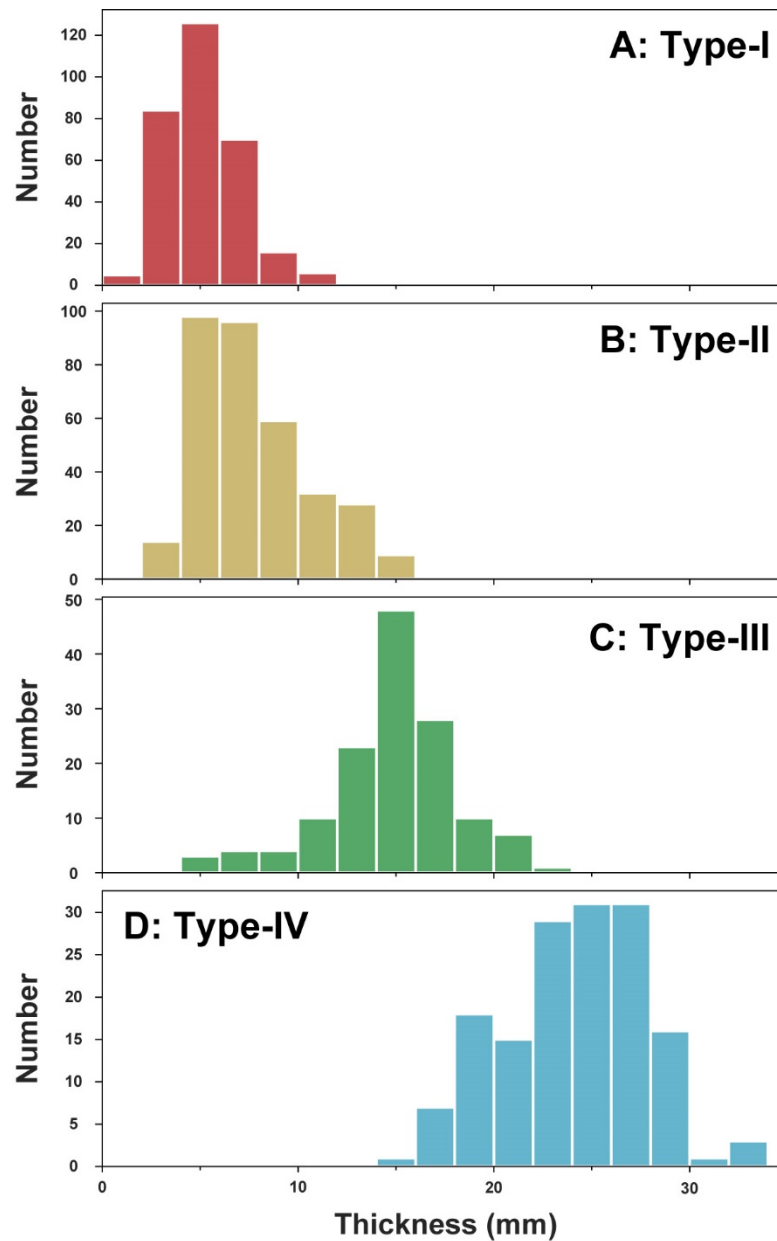


Figure 8. Histograms of oxide layer thickness in nodule samples: (A) Type-I, (B) Type-II, (C) Type-III, and (D) Type-IV nodules.

Figure 9 shows the abundance ratios of Type I, II, III, and IV nodules at each dive site. Except for 6 K #1460 and 1503, where only a few samples were collected (Table 1), at least two types of nodule samples were collected from all the other dive sites. All types of nodules were sampled at eight of 11 sites (Figure 9). This means that the nodules in the study area started to grow at any time; that is, they did not start growing simultaneously. However, histograms of the distribution of oxide layer thickness in the nodules showed distinct peaks at each site (Figure 10). This suggested that the onset of nodule growth was not continuous, but rather an event triggered the growth of more nodules. In addition, multiple peaks in the thickness distribution in nodules from many sites were identified (Figure 10), indicating that nodule growth was initiated often, even within a single site.

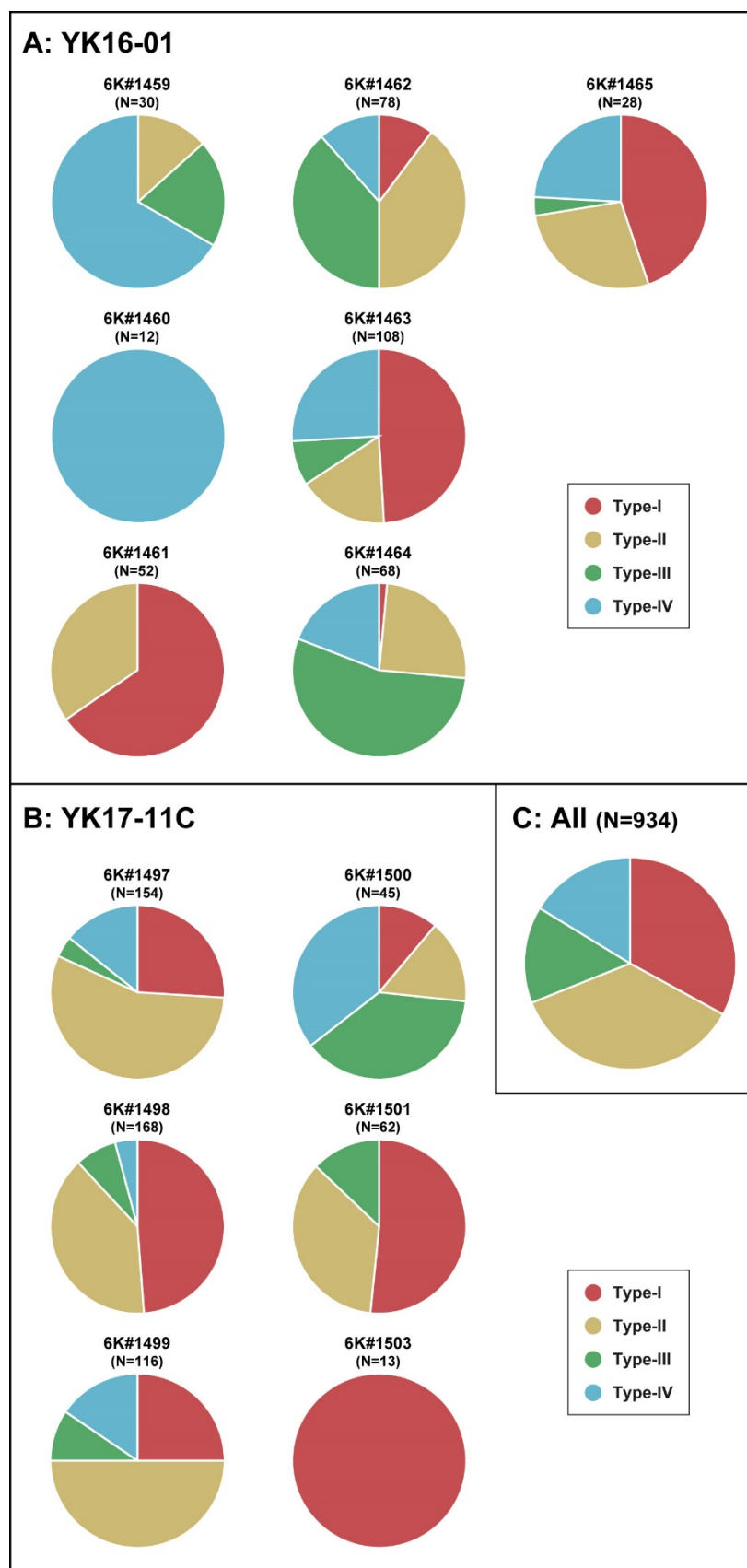


Figure 9. Pie charts show relative amounts of four types of nodule samples. Sample were collected at (A) YK16-01, (B) YK17-01C, and (C) all dive sites.

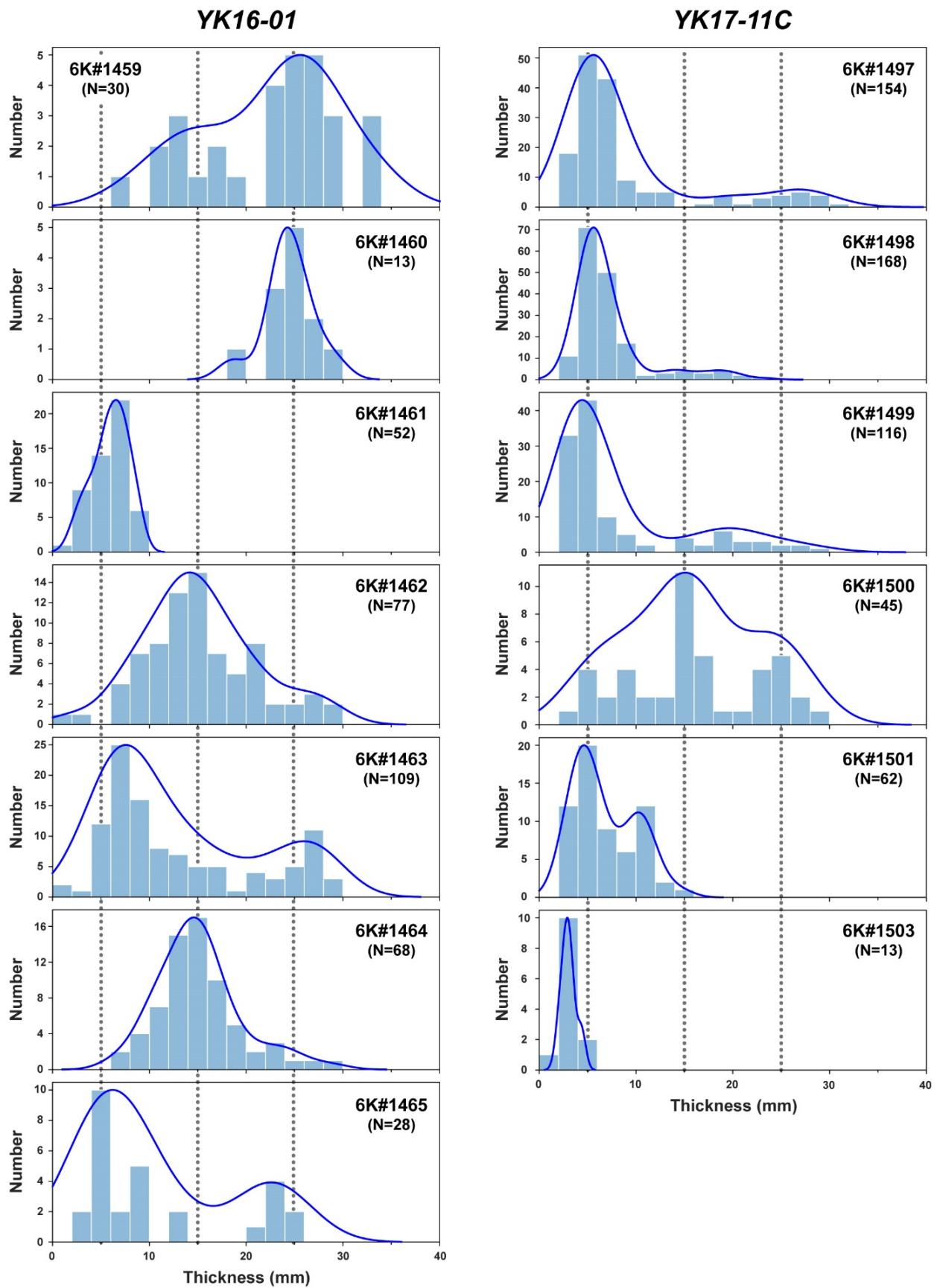


Figure 10. Histograms and corresponding Kernel density estimates (KDE) show distribution of oxide layer thickness in nodule samples collected from all dive sites. Dashed vertical lines, positions of peaks that are common to all sites.

An overview of the histograms of total layer thickness for all sites shows three prominent peaks (5, 15, and 25 mm) that were common to several sites (Figure 10). Peaks at 5, 15, and 25 mm were recognized at eight (6K#1461, 1463, 1465, 1497, 1498, 1499, and 1501), four (6K#1459, 1462, 1464, and 1500), and four sites (6K#1459, 1463, 1465, 1500), respectively (Figure 10). These peaks were evident between sites that were more than 100 km apart (for example, the 15-mm peak at 6 K #1462, 1464, and 1500; Figure 1). These three common peaks suggested that at least three extensive events covering hundreds of kilometers triggered the formation of ferromanganese nodules in the study area.

However, a closer look revealed that the ratio of each type of nodule occurrence considerably varied among dive sites (Figure 9). For example, Type I nodules are dominant at 6 K #1461, 1463, 1465, 1498, and 1501, whereas Type II nodules were most common at 6 K #1497 and 1499. In addition, Types III and IV nodules were most common at 6 K #1464 and 1459, respectively. Moreover, reflecting the difference in the dominant nodule type, the distribution of oxide layer thickness also differed among dive sites, even though the peaks were at the same positions (Figure 10). Such differences can be recognized even for nearby sites within tens of kilometers (6 K #1459 and 1501, 6 K #1461 and 1464, 6 K #1462 and 1497) (Figure 1). This suggested that heterogeneous local events led to nodule growth initiation. We therefore considered that local phenomena on the order of tens of kilometers affected the occurrence and distribution of ferromanganese nodules in addition to the broader events described above.

4. Conclusions

X-ray CT analysis of the structures of the oxide layer of 934 ferromanganese nodule samples collected from the western North Pacific Ocean around Minamitorishima Island provided the following results:

1. The oxide layer of the nodules essentially grew isotropically, regardless of direction. This indicated that nodule shape depended primarily on the shape of the nucleus.
2. The oxide layer of the nodules can be subdivided from outside to inside based on CT numbers into sublayers I and II, III, and IV. These were comparable to the layers identified by Machida et al. [12] based on physiological findings as follows: sublayer I corresponded to L0, sublayer II to L1, and III and IV to L2.
3. We identified Types I–IV nodule samples with only sublayer I, or and with sublayers I and II, I–III, and I–IV, respectively. The number of sublayers correlated with the total thickness of the oxide layer, indicating that both can represent the relative age of nodules.
4. Almost all types of nodules were found at the investigated sites. This indicated that the nodules in the study area did not start growing simultaneously, but comprised a mixture that started growing at different times.
5. Histograms of oxide layer thickness revealed three peaks that were prevalent throughout the study area, indicating that at least three widespread events covering several hundred kilometers triggered ferromanganese nodule generation in this region.
6. The dominant types of nodules noticeably differed among dive sites that were only a few dozen kilometers apart. This suggests that local factors on a scale up to tens of kilometers also affects the onset of nodule growth and distribution.

Future research is expected to provide further insights into the genesis and formation history of ferromanganese nodules in the Minamitorishima EEZ by adding data on the detailed chemical composition and formation age of each sublayer to the CT results.

Supplementary Materials: The following are available online at <https://www.mdpi.com/article/10.3390/min11101100/s1>, Table S1: Innermost sublayer, weight, size, and oxide layer thickness of ferromanganese nodules collected during YK16-02 and YK17-11C cruises.

Author Contributions: Conceptualization, K.N.; methodology, S.M., D.T. and R.S.; formal analysis, D.T., R.S. and K.N.; investigation, D.T., R.S. and K.N.; resources, K.N., K.Y., K.F. and Y.K.; data curation, D.T. and K.N.; writing—original draft preparation, K.N., D.T. and R.S.; writing—review

and editing, all authors; visualization, D.T., R.S. and K.N.; supervision, K.N. and Y.K.; project administration, K.N.; funding acquisition, K.N., S.M. and Y.K. All authors have read and agreed to the published version of the manuscript.

Funding: This research was funded by the cross-ministerial Strategic Innovation Promotion Program (SIP) “Innovative Technology for Exploration of Deep-Sea Resources” (Lead agency: JAMSTEC) and Japan Society for the Promotion of Science (JSPS) through the Grant-in-Aid Scientific Research (S) No. 15H05771, (A) No. 17H01361, and (A) No. 21H04667.

Data Availability Statement: Data are shown in all figures and tables of the main text and in the Supplementary Materials. Raw data of X-ray CT can be provided from the corresponding author upon request.

Acknowledgments: We thank the Shinkai 6500 operation team and the crew of the R/V Yokosuka for their skillful support during the YK16-01 and YK17-11C cruises. The research cruises were conducted in the SIP of Japan. We are also grateful to N. Ahagon, R. Yamaoka, T. Yabuki, and K. Yoshida for their assistance with the X-ray CT scanning.

Conflicts of Interest: The authors declare no conflict of interest. The funders had no role in the design of the study; in the collection, analyses, or interpretation of data; in the writing of the manuscript, or in the decision to publish the results.

References

1. Hein, J.R.; Petersen, S. The geology of manganese nodules. In *Deep Sea Minerals: Manganese Nodules: A Physical, Biological, Environmental and Technical Review*; Baler, E., Beaudoin, Y., Eds.; Secretariat of the Pacific Community: Noumea, New Caledonia, 2013; Volume 1B, pp. 7–18.
2. Hein, J.R.; Koschinsky, A. Deep-Ocean Ferromanganese Crust and Nodules. In *Earth Systems and Environmental Sciences, Treatise on Geochemistry*, 2nd ed.; Holland, H., Turekian, K., Eds.; Elsevier: Amsterdam, The Netherlands, 2013; pp. 273–291.
3. Hein, J.R.; Koschinsky, A.; Kuhn, T. Deep-ocean polymetallic nodules as a resource for critical materials. *Nat. Rev. Earth Environ.* **2020**, *1*, 158–169. [[CrossRef](#)]
4. Hein, J.R.; Mizell, K.; Koschinsky, A.; Conrad, T.A. Deep-ocean mineral deposits as a source of critical metals for High and green-technology applications: Comparison with land-based resources. *Ore Geol. Rev.* **2013**, *51*, 1–14. [[CrossRef](#)]
5. Halbach, P.; Scherhag, C.; Hebisch, U.; Marchig, V. Geochemical and Mineralogical Control of Different Genetic Types of Deep-Sea Nodules from the Pacific Ocean. *Mineral. Depos.* **1981**, *16*, 59–84. [[CrossRef](#)]
6. Banakar, V.K.; Pattan, J.N.; Jauhari, P. Size, Surface Texture, Chemical Composition and Mineralogy Interrelations in Ferromanganese Nodules of Central Indian Ocean. *Indian J. Mar. Sci.* **1989**, *18*, 201–203.
7. Usui, A.; Nishimura, A.; Mita, N. Composition and Growth History of Surficial and Buried Manganese Nodules in the Penrhyn Basin, Southwestern Pacific. *Mar. Geol.* **1993**, *114*, 133–153. [[CrossRef](#)]
8. von Stackelberg, U. Growth History of Manganese Nodules and Crusts of the Peru Basin. In *Geological Society London Special Publications*; Nicholson, K., Hein, J.R., Buhn, B., Dasgupta, S., Eds.; Geological Society: London, UK, 1997; Volume 119, pp. 153–176.
9. von Stackelberg, U.; Beiersdorf, H. The Formation of Manganese Nodules Between the Clarion and Clipperton Fracture Zones Southeast of Hawaii. *Mar. Geol.* **1991**, *98*, 411–423. [[CrossRef](#)]
10. Wegorzewski, A.V.; Kuhn, T. The Influence of Suboxic Diagenesis on the Formation of Manganese Nodules in the Clarion Clipperton Nodule Belt of the Pacific Ocean. *Mar. Geol.* **2014**, *357*, 123–138. [[CrossRef](#)]
11. Wegorzewski, A.V.; Grangeon, S.; Webb, S.M.; Heller, C.; Kuhn, T. Mineralogical Transformations in Polymetallic Nodules and the Change of Ni, Cu and Co Crystal-Chemistry Upon Burial in Sediments. *Geochim. Cosmochim. Acta* **2020**, *282*, 19–37. [[CrossRef](#)]
12. Machida, S.; Fujinaga, K.; Ishii, T.; Nakamura, K.; Hirano, N.; Kato, Y. Geology and geochemistry of ferromanganese nodules in the Japanese Exclusive Economic Zone around Minamitorishima Island. *Geochem. J.* **2016**, *50*, 539–555. [[CrossRef](#)]
13. Machida, S.; Sato, T.; Yasukawa, K.; Nakamura, K.; Iijima, K.; Nozaki, T.; Kato, Y. Visualisation method for the broad distribution of seafloor ferromanganese deposits. *Mar. Georesources Geotechnol.* **2019**, *39*, 267–279. [[CrossRef](#)]
14. Ohtani, T.; Nakashima, Y.; Muraoka, H. Three-Dimensional Mirolitic Cavity Distribution in the Kakkonda Granite From Borehole WD-1a Using X-Ray Computerized Tomography. *Eng. Geol.* **2000**, *56*, 1–9. [[CrossRef](#)]
15. Hirono, T.; Takahashi, M.; Nakashima, S. In Situ Visualization of Fluid Flow Image Within Deformed Rock by X-Ray CT. *Eng. Geol.* **2003**, *70*, 37–46. [[CrossRef](#)]
16. Cnudde, V.; Masschaele, B.; Dierick, M.; Vlassenbroeck, J.; VanHoorebeke, L.V.; Jacobs, P. Recent Progress in X-Ray CT as a Geosciences Tool. *Appl. Geochem.* **2006**, *21*, 826–832. [[CrossRef](#)]
17. Duluu, O.G.; Tufan, M.S.; Szobotka, S.A. Computer Axial Tomography Investigation of Polymetallic Nodules. *Mar. Geol.* **1997**, *138*, 303–311. [[CrossRef](#)]
18. Benites, M.; Millo, C.; Hein, J.R.; Nath, B.; Murton, B.J.; Galante, D.; Jovane, L. Integrated Geochemical and Morphological Data Provide Insights Into the Genesis of Ferromanganese Nodules. *Minerals* **2018**, *8*, 488. [[CrossRef](#)]

19. Keller, A. High Resolution, Non-Destructive Measurement and Characterization of Fracture Apertures. *Int. J. Rock Mech. Min. Sci.* **1998**, *35*, 1037–1050. [[CrossRef](#)]
20. Van Geet, M.; Swennen, R.; Wevers, M. Quantitative Analysis of Reservoir Rocks by Microfocus X-Ray Computerised Tomography. *Sediment. Geol.* **2000**, *132*, 25–36. [[CrossRef](#)]
21. Van Geet, M.; Swennen, R.; Wevers, M. Towards 3-D Petrography: Application of Microfocus Computer Tomography in Geological Science. *Comput. Geosci.* **2001**, *27*, 1091–1099. [[CrossRef](#)]
22. Ketcham, R.A.; Carlson, W.D. Acquisition, Optimization and Interpretation of X-Ray Computed Tomographic Imagery: Applications to the Geosciences. *Comput. Geosci.* **2001**, *27*, 381–400. [[CrossRef](#)]
23. Mogensen, K.; Stenby, E.H.; Zhou, D. Studies of Water Flooding in Low-Permeable Chalk by Use of X-Ray CT Scanning. *J. Petrol. Sci. Eng.* **2001**, *32*, 1–10. [[CrossRef](#)]
24. Akin, S.; Kovscek, A.R. Computed Tomography in Petroleum Engineering Research. In *Geological Society London Special Publications*; Mees, F., Swennen, R., Van Geet, M., Jacobs, P., Eds.; Geological Society: London, UK, 2003; Volume 215, pp. 23–38.
25. Rosset, A.; Spadola, L.; Ratib, O. OsiriX: An Open-Source Software for Navigating in Multidimensional DICOM Images. *J. Digit. Imaging* **2004**, *17*, 205–216. [[CrossRef](#)] [[PubMed](#)]
26. Kim, G.; Jung, H.J.; Lee, H.J.; Lee, J.S.; Koo, S.; Chang, S.H. Accuracy and Reliability of Length Measurements on Three-Dimensional Computed Tomography Using Open-Source OsiriX Software. *J. Digit. Imaging* **2012**, *25*, 486–491. [[CrossRef](#)] [[PubMed](#)]
27. Machida, S.; Nakamura, K.; Kogiso, T.; Shimomura, R.; Horinouchi, K.; Okino, K.; Kato, Y. Fine-Scale Chemostratigraphy of Cross-Sectioned Hydrogenous Ferromanganese Nodules From the Western North Pacific. *Isl. Arc.* **2021**, *30*, 12395. [[CrossRef](#)]